Composites Part C: Open Access 4 (2021) 100089

Contents lists available at ScienceDirect

Composites Part C: Open Access

journal homepage: www.elsevier.com/locate/jcomc

On the effective elastic properties based on mean-field homogenization of sheet molding compound composites

A. Trauth [a,c,*], L. Kehrer [b], P. Pinter [a], K. Weidenmann [a,c], T. Böhlke [b]

[a] Karlsruhe Institute of Technology (KIT), Institute for Applied Materials, Karlsruhe, Germany
[b] Karlsruhe Institute of Technology (KIT), Institute of Engineering Mechanics, Chair for Continuum Mechanics, Karlsruhe, Germany
[c] Augsburg University, Institute of Materials Resource Management, Chair of Hybrid Composite Materials, Augsburg, Germany

ARTICLE INFO

Keywords:
Sheet molding compound
Mean-Field homogenization
Hashin-Shtrikman two-step method
Computed tomography
Orientation analysis
Mechanical testing

ABSTRACT

Fiber reinforced polymers, for example sheet molding compounds (SMC), have gained significant importance as lightweight materials. In this work, a SMC composite based on unsaturated polyester-polyurethane hybrid resin (UPPH) reinforced with discontinuous long glass fibers is considered. The mechanical behavior of this composite is highly governed by its microstructure. Based on samples extracted from compression molded sheets, the underlying microstructure is characterized by means of X-ray computed tomography (μCT) scans. Tensile tests are performed to investigate and characterize the elastic properties of this composite. A mean-field method is presented to approximate the effective elastic behavior. In this context, the tensile tests performed serve as validation data for the simulation results. The effective Young's modulus is in good agreement with the experimentally obtained data with a deviation less than 15%.

1. Introduction

Fiber reinforced polymers offer advantageous properties for numerous technical applications based on their high specific stiffness and strength. Among this material class, sheet molding compounds additionally stand out due to low material and manufacturing costs [1–3]. Manufacturing starts with production of semi-finished sheets, which are compression molded to the final geometry in a subsequent manufacturing step. Closure of the mold heats the stack of semi-finished material, reduces its viscosity and forces the material to fill the mold. Complex flow phenomena lead to anisotropic fiber orientation and fiber distribution [4]. Fibers most preferably align along the in-plane flow direction within the core. Fibers in the shell layers may bend, disaggregate and spread [5]. Fiber orientation distribution significantly affects resulting material properties [6,7], hence performance of the materials is strongly affected by the microstructure. Considering tensile properties, Boylan et al. [8] investigated tensile properties of unsaturated polyester-based SMC composites, which featured a fiber volume content of 21%, indicating that observed anisotropic mechanical material properties for SMC sheets resulted from material flow during compression molding. A substantial in-plane anisotropy in terms of tensile stiffness and strength was also observed in [9]. Whereas material flow during compression molding is seen to importantly affect fiber orientation and hence material performance, even SMC materials, which did not flow during molding (hence 100% mold coverage was realized for compression molding), showed anisotropic material properties [10]. This effect was linked to the movement of the conveyor belt during the manufacturing of the semi-finished sheets.

Sheet molding compounds, in combination with bulk molding compounds had the highest economic importance in terms of production volume in Europe in the last few years [11]. To further implement components made from sheet molding compounds, modeling of material behavior can significantly reduce development time. Recent approaches focus on the simulation of flow-induced fiber orientation [12,13] and the consideration of microstructural characteristics to predict material behavior and damage [14–16]. A first attempt to realize a virtual process chain for sheet molding compound composites was established and validated by means of experimental investigations on a demonstrator structure [17,18]. For fiber reinforced materials, the objective of mean-field methods is to predict the behavior of the composite on a macrostructural level taking the heterogeneities on the microstructure into account. Commonly, the mean-field methods are divided into bounding and estimating methods. Upper and lower bounds for polycrystalline composites were formulated by [19,20], respectively. Closer, second-order bounds were developed by [21]. Known representatives of the estimating methods are the self-consistent scheme, first introduced by [22,23], and the Mori-Tanaka method [24]. In order to determine a precise prediction, a detailed description of the underlying microstructure of a fibrous composite is necessary including the geometrical description as well as the spatial and orientation distribution of the fibers. Some homogenization methods take the fiber orientation into account either based on a dis-

* Corresponding author.
E-mail address: anna.trauth@mrm.uni-augsburg.de (A. Trauth).

https://doi.org/10.1016/j.jcomc.2020.100089
Received 22 October 2020; Received in revised form 8 December 2020; Accepted 14 December 2020

crete fiber orientation description [25], on orientation distribution functions [26], or by using a mean fiber orientation measure in terms of orientation tensors [27,28]. Due to their mathematical simple structure, orientation tensors provide a numerical efficient description of the microstructure. Moreover, they can be determined directly based on μCT scans.

In contrast to mean-field methods, full-field methods can be used to compute the overall behavior based on the fully resolved microstructure. In this context, a boundary value problem for a representative volume element or a unit cell is solved. For this purpose, finite element [17,29], or fast Fourier [30,31] methods are commonly used. By volume averaging of the local solutions, the homogenized properties are determined. Applications of a fast Fourier method in the context of phase field fracture problems is given in [32]. In [33], a gradient-based solver is developed which is directly applied to inelastic problems.

In this work, a Hashin-Shtrikman based two-step method is formulated by means of orientation tensors and a variable reference stiffness. In this context, a tailored approach is developed that is favorable in terms of composite structures with a high phase contrast. By comparing the effective behavior of the composite with experimental data, the predictability can be quantified.

Outline. The work at hand is structured as follows. In Section 2, the composite material is introduced and the specifications are given. The microstructure characterization by computed tomography scans is outlined in Section 3. Furthermore, the mechanical characterization based on tensile tests is described. Moreover, the mean-field method for the prediction of the elastic material properties is briefly presented. In Section 4, the results of the orientation analysis are shown. The subsequently presented experimental results of the tensile tests are discussed in detail. Additionally, the computed elastic Young's modulus is compared with the experimental tensile data. Finally, in Section 5, a summary of the main results is given and conclusions are drawn.

Notation. A direct tensor notation is preferred as in [34,35]. Scalars are denoted by lowercase letters, e.g. a, and vectors by lowercase bold letters, e.g. $\boldsymbol{a}$. Second-order and fourth-order tensors are indicated by $\boldsymbol{A}$ and $\mathbb{A}$, respectively. The scalar product and the dyadic product are given by $\boldsymbol{A} \cdot \boldsymbol{B}$ and $\boldsymbol{A} \otimes \boldsymbol{B}$. Using $\boldsymbol{A}\boldsymbol{B}$ and $\mathbb{A}\mathbb{B}$, respectively, the composition of two tensors of the same order is denoted. A linear mapping is given by $\boldsymbol{A} = \mathbb{C}[\boldsymbol{B}]$. By means of $\mathbb{A}^{\mathsf{T}_\mathsf{H}}$, the major transposition of a fourth-order tensor is given, defined by $A^{\mathsf{T}_\mathsf{H}}_{ijkl} = A_{klij}$ in index notation. Moreover, $\mathbb{A}^{\mathsf{T}_\mathsf{R}}$ denotes the minor transposition with respect to the right subindizes, reading $A^{\mathsf{T}_\mathsf{R}}_{ijkl} = A_{ijlk}$ in index notation. The quantities $\boldsymbol{I}$ and $\mathbb{I}^{\mathsf{S}}$ denote the identity tensors on symmetric tensors of second- and fourth-order, respectively. The brackets $\langle\cdot\rangle$ are defined as ensemble average that corresponds to volume average in the infinite volume limit for ergodic media.

2. Material

The investigated glass fiber reinforced sheet molding compound is based on an unsaturated polyester-polyurethane hybrid two-step curing resin system. No fillers are added. Manufacturing and investigation of this specific SMC composite took place within the International Research Training Group "Integrated engineering of continuous-discontinuous long fiber reinforced polymer structures". Manufacturing of the SMC material is also described in [36], for example. The detailed composition of the SMC including the resin system is listed in Table 1.

The semi-finished SMC sheets are manufactured on a flat conveyor belt (type: HM-LB-800 by Schmidt and Heinzmann) at Fraunhofer ICT in Pfinztal, Germany. The resin is deposited onto a polymeric film. The reinforcing fibers are cut by a cutting unit to bundles featuring a length of 25.4 mm and drop onto the paste layer, which is then covered with a second polymeric film and resin to form a sandwich or SMC mat. Compression molding is realized with a press (type: COMPRESS PLUS DCP-G 3600/3200 AS by Dieffenbacher) at approximately 150 °C mold temperature, 2500 kN, and 112 s mold closing time. The stack of semi-finished SMC is placed in the center of a rectangular shaped mold, featuring a section of 250 × 800 mm^2, with a mold coverage of approximately 35%. Hence, the semi-finished SMC is forced to unidirectionally flow to fill the mold. The discontinuous glass fiber reinforced SMC sheets feature a nominal thickness of 3 mm. Specimens for experimental investigation, with the dimensions of 100 × 15 mm^2, are extracted by water jet cutting from charge and flow region in 0° and 90° with 0° coinciding the direction of flow.

Table 1
Resin components and fiber type of discontinuous glass fiber SMC.

Component	Product name	Supplier
UPPH resin	Daron ZW 14141	Aliancys
Release agent	BYK 9085	BYK
De-airing	BYK-A-530	BYK
Inhibitor	pBQ	Fraunhofer ICT
Peroxide	Trigonox 117	Akzonobel
Thickener (Isocyanate)	Lupranat M20R	BASF
Fiber (41wt% [nom.])	Multistar 272	Johns Manville

Table 2
Image acquisition parameters of CT scans.

Acquisition parameter	value
Acceleration voltage	100 kV
Tube current	0.05 mA
Focus-object distance	31.27 mm
Focus-detector distance	749.97 mm
Voxel size	8.04 μm
Integration time / Pixel binning	500 ms / 1
Number of projections	2400

3. Methods

3.1. Microstructure characterization

Important characteristics of the SMC material at hand are the fiber volume content, the fiber orientation and the fiber length distribution. As the SMC process does not degrade the fiber length in a significant manner, it is appropriate to consider the adjusted length of 25.4 mm corresponding to the blade distance of the cutting unit for mechanical models.

To determine the fiber volume content (FVC) of the discontinuous SMC sheets, circular specimens with a diameter of 20 mm are extracted from different locations of the sheets and a thermogravimetric analysis (TGA) is performed with a Leco TGA701 (LECO Corporation, St. Joseph, MI, USA) at the Fraunhofer ICT in Pfinztal, Germany. Thermogravimetric analyses generally enable to determine the fiber weight content by incinerating the matrix of a specimen and with the mass density of the matrix material (ρ_M=1.14 g/cm^3) and the fibers (ρ_F= 2.6 g/cm^3) the fiber volume content of the specimen can be determined. For the investigation of the discontinuous glass fiber SMC the chamber is heated up to 550°C with a heating rate of 37°C min^{-1}. The dwell temperature remains constant for 2 h while the weight loss is tracked.

Fiber orientation distributions are extracted from micro computed tomography scans by an "YXLON CT Precision" device. All scans are acquired using a transmission tube with tungsten target and a Perkin Elmer detector with a resolution of 2048 × 2048 pixels^2 at a pixel pitch of 0.2 mm. Further scanning parameters are listed in Table 2. Volume images are reconstructed using the in-build reconstruction algorithm by YXLON resulting in a three-dimensional scalar gray value image I.

The local fiber orientation is evaluated in each voxel $\alpha = 1 \dots M$ by an algorithm based on the structure tensor [37,38]. Assuming a prior

segmentation between fibers and matrix, based on the structure tensor, the average gradient direction in the vicinity of a point x on a fiber can be computed and stored as a normalized vector in each voxel, leading to the fiber orientation distribution. Orientation statistics are created considering only fiber voxels with gray values larger than the threshold t, which is calculated from the gray value histogram by a moments preserving method by Tsai [39].

To describe fiber orientation states, an orientation density function $\psi(\boldsymbol{n})$, referred to as orientation distribution function (ODF), is introduced, cf. [40].

The volume fraction of fibers with orientation $\boldsymbol{n}$ is specified by the ODF, i.e., $\mathrm{d}v(\boldsymbol{n})/v = \psi(\boldsymbol{n})\mathrm{d}S$. Here, $\mathrm{d}S$ denotes the surface element $\mathrm{d}S = \sin(\theta)\,\mathrm{d}\theta\,\mathrm{d}\varphi/(4\pi)$, with the azimuthal angle θ and the polar angle φ, on a unit sphere $S = \{\boldsymbol{n} \in \mathbb{R}^3 : \|\boldsymbol{n}\| = 1\}$, cf. [41]. The ODF is non-negative, normalized, and centrosymmetric, i.e.,

$$\psi(\boldsymbol{n}) \geq 0, \quad \int_S \psi(\boldsymbol{n})\mathrm{d}S = 1, \quad \psi(\boldsymbol{n}) = \psi(-\boldsymbol{n}). \tag{1}$$

Moreover, the ODF provides one-point statistical information on the composite, cf. [42].

According to [43], the fiber orientation state can be represented by fiber orientation tensors of second and fourth order which are moment tensors of the ODF referred to as orientation tensors of the first kind. The continuous orientation tensors of second and fourth order are computed by

$$\boldsymbol{N} = \int_S \boldsymbol{n} \otimes \boldsymbol{n}\, \psi(\boldsymbol{n})\, \mathrm{d}S \tag{2}$$

and

$$\mathbb{N} = \int_S \boldsymbol{n} \otimes \boldsymbol{n} \otimes \boldsymbol{n} \otimes \boldsymbol{n}\, \psi(\boldsymbol{n})\, \mathrm{d}S. \tag{3}$$

For discrete CT-data the empirical orientation tensors are calculated by a voxel-based averaging scheme

$$\boldsymbol{N} = \frac{1}{\sum_{\alpha=1}^{M} w_\alpha} \sum_{\alpha=1}^{M} w_\alpha\, \boldsymbol{n}_\alpha \otimes \boldsymbol{n}_\alpha \tag{4}$$

and

$$\mathbb{N} = \frac{1}{\sum_{\alpha=1}^{M} w_\alpha} \sum_{\alpha=1}^{M} w_\alpha\, \boldsymbol{n}_\alpha \otimes \boldsymbol{n}_\alpha \otimes \boldsymbol{n}_\alpha \otimes \boldsymbol{n}_\alpha \tag{5}$$

with

$$w_\alpha = \begin{cases} 1 & \text{if } I(\alpha) > t \\ 0 & \text{else.} \end{cases} \tag{6}$$

The quantity w_α is a weighting factor which is either one when the gray value threshold t is exceeded or zero if not. M defines the absolute number of voxels in the image. Hence, a voxel-weighted orientation tensor is calculated, which is equivalent to a volume-weighting neglecting the influence of the discretization by the voxel grid. Tests with artificial data showed that the influence by the discretization is low [38,44]. Moreover, the weighting by voxels or volume and length is equivalent assuming a constant fiber diameter.

3.2. Macrostructure characterization – tensile testing

Tensile tests are carried out in a conditioned laboratory at 23°C on a ZMART.PRO universal testing machine by ZwickRoell with a load cell capacity of 200 kN. Before testing, specimens were hydraulically clamped with a clamping distance of 50 mm and preloaded with $F_p \approx 90$ N to level out any compressive loads resulting due to clamping. Each specimen is loaded up to a maximum elongation of 0.35% and unloaded to F_p. The loading-unloading cycle is repeated three times with a nominal loading rate of 0.1 mm min^{-1}. Strains are measured with a tactile extensometer within a gauge section of 20 mm (cf. Fig. 1). Tensile modulus of elasticity (E_t) is determined with a least squares method in the strain range of 0.05%–0.25% from the loading and unloading phase, respectively. As shown by [45], mechanical properties of specimens, extracted from the edges of a SMC sheet are inferior to mechanical properties of specimens extracted from the center, due to formation of resin rich regions resulting from outward flow of the resin during molding. In addition, deformation of fiber bundles is more severe at the edges of the sheet [46], which might also affect mechanical performance. To account for this point, specimens for mechanical characterization within this study were extracted with appropriate distance from the edges of the manufactured SMC sheets.

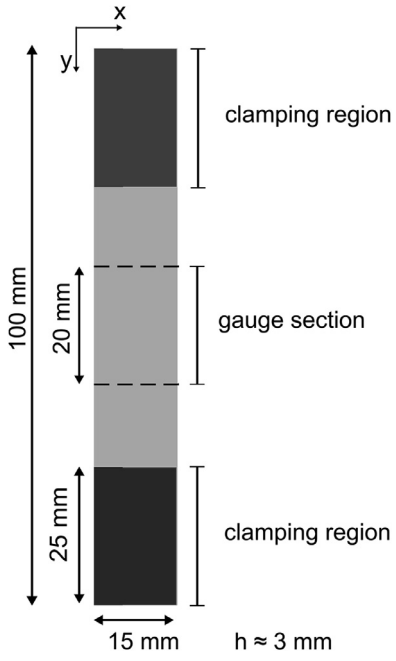

Fig. 1. Tensile test specimen.

3.3. Mean-field homogenization

To compute the effective elastic material properties of the SMC composite, the two-step Hashin-Shtrikman mean-field homogenization method is used. This method is based on the eigenstrain formulation proposed in [47,48]. In this context, a two-phase composite is assumed to contain N fibers, embedded in a polymeric matrix. In a first step, the microstructure is partitioned into domains with fibers of a certain orientation. This results into as many domains as there are differently oriented fibers within the microstructure.

The matrix material is denoted by $(\cdot)_\mathrm{M}$, and the fiber material by $(\cdot)_\alpha$. Moreover, $\mathbb{C}_\mathrm{M}$ denotes the matrix stiffness, whereas $\mathbb{C}_\alpha$ represents the fiber stiffness in domain α. The fiber and matrix material are assumed to exhibit isotropic material properties. The effective elastic properties for each domain $\bar{\mathbb{C}}_\alpha^{\mathrm{UD}\pm}$ are determined by applying the upper and lower Hashin-Shtrikman bounds reading

$$\bar{\mathbb{C}}_\alpha^{\mathrm{UD}+} = \mathbb{C}_\alpha + c_\mathrm{M}(\mathbb{C}_\mathrm{M} - \mathbb{C}_\alpha)(\mathbb{I}^\mathrm{S} + c_\alpha \mathbb{P}_\alpha^\mathrm{UD}(\mathbb{C}_\mathrm{M} - \mathbb{C}_\alpha))^{-1}, \tag{7}$$

$$\bar{\mathbb{C}}_\alpha^{\mathrm{UD}-} = \mathbb{C}_\mathrm{M} + c_\alpha(\mathbb{C}_\alpha - \mathbb{C}_\mathrm{M})(\mathbb{I}^\mathrm{S} + c_\mathrm{M} \mathbb{P}_\alpha^\mathrm{UD}(\mathbb{C}_\alpha - \mathbb{C}_\mathrm{M}))^{-1}. \tag{8}$$

The fiber volume fraction is denoted by c_α holding $c_\mathrm{M} + \sum_{\alpha=1}^{N} c_\alpha = 1$ true. For the special case of unidirectional fibers, Hill's polarization tensor $\mathbb{P}_\alpha^\mathrm{UD}$ is explicitly given, cf. [47,49]. In the second step, the transversely isotropic domains are homogenized by applying the Hashin-Shtrikman procedure to the pseudo-grain-like structure, reading

$$\begin{aligned} \bar{\mathbb{C}}^{\mathrm{HS}\pm} = \langle \bar{\mathbb{C}}^{\mathrm{UD}\pm} \mathbb{A} \rangle &= \mathbb{C}_0 - \mathbb{P}_0^{-1} + \langle (\mathbb{P}_0^{-1} + \bar{\mathbb{C}}^{\mathrm{UD}\pm} - \mathbb{C}_0)^{-1} \rangle^{-1} \\ &= \mathbb{C}_0 - \mathbb{P}_0^{-1} + \langle \mathbb{A}^* \rangle_\mathrm{oa}^{-1}. \end{aligned} \tag{9}$$

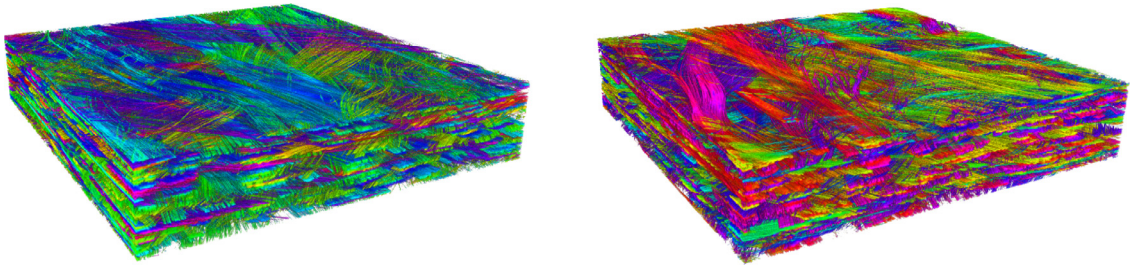

Fig. 2. Specimen 0°_{1} (left) and specimen 90°_{1} (right). The edge length of each image regions is 9 mm.

Table 3
Fiber volume content of investigated samples.

Plate ID	Fiber volume content (mean value and standard deviation in %)
1	24.2±0.9
2	26.4±1.1
3	26.1±1.2
4	25.7±1.3
5	27.5±1.6
6	27.8±0.8
7	21.5±1.4

Hill's polarization tensor $\mathbb{P}_0$ in the last equation can be specified according to modeling assumptions with respect to the geometry and the distribution of the domains. In this context, an isotropic two-point correlation of the domains is assumed for which $\mathbb{P}_0$ corresponds to the spherical polarization tensor, cf. [47]. An ellipsoidal two-point correlation would also be possible, for simplicity, here, the isotropic two-point correlation has been used. Eq. (9) is given in terms of the reference stiffness $\mathbb{C}_0$ which is chosen between the matrix and the fiber stiffness reading

$$\mathbb{C}_0 = (1-k)\mathbb{C}_{\mathrm{M}} + k\mathbb{C}_{\mathrm{F}}, \quad k \in [0,1]. \tag{10}$$

The quantity $\mathbb{A}$ denotes the strain localization tensor [21]. Since the expression $\mathbb{A}^*$ has a transversely isotropic symmetry, orientation tensors of second and fourth order can be used to account for the orientation distribution of the fibers, cf. [43]. Thus, the orientation average is computed by

$$\begin{aligned}\langle \mathbb{A}^* \rangle_{\mathrm{oa}} = b_1 \mathbb{N} + b_2(\boldsymbol{N}\otimes\boldsymbol{I} + \boldsymbol{I}\otimes\boldsymbol{N}) + b_3(\boldsymbol{N}\square\boldsymbol{I} + (\boldsymbol{N}\square\boldsymbol{I})^{\mathsf{T_R}} \\ + (\boldsymbol{I}\square\boldsymbol{N})^{\mathsf{T_H}} + (\boldsymbol{I}\square\boldsymbol{N})^{\mathsf{T_R}}) + b_4\boldsymbol{I}\otimes\boldsymbol{I} + b_5\mathbb{I}^{\mathrm{S}},\end{aligned} \tag{11}$$

with the coefficients $b_1 = A^*_{1111} + A^*_{2222} - 2A^*_{1122} - 4A^*_{1212}$, $b_2 = A^*_{1122} - A^*_{2233}$, $b_3 = A^*_{1212} + (A^*_{2233} - A^*_{2222})/2$, $b_4 = A^*_{2233}$ and $b_5 = A^*_{2222} - A^*_{2233}$. A detailed description can be found in [28].

4. Results and discussion

4.1. Microstructure characterization

The fiber volume content of each plate, determined by means of thermogravimetric analysis, is listed in Table 3.

Results of the orientation analysis are illustrated three dimensionally in Fig. 2. It can readily be seen that the fibers are arranged in bundles which are slightly dispersed on the surface of the sample. Fig. 3 depicts the center slice of the same datasets in 2D. The principal orientation can be seen and by comparing the color of the fibers with the color wheel on the lower right of the image, it is possible to judge about the reliability of the algorithms.

The graphs in Figs. 4 and 5 show the components of the orientation tensors over the thickness direction. Since the z-component is very small (z−axis refers to the thickness of the specimen), only N_{xx}, N_{yy} and N_{xy} are plotted. Nevertheless, it is possible to derive the N_{zz} component from the data as the trace of the orientation tensor is one. Both curves indicate for an anisotropic material while the component of the orientation tensor which is aligned in flow direction is higher than the other. Furthermore, the data suggests that there is a slight skin-core effect due to a higher orientation in flow direction on the edges. However, the effect is less distinct as e.g. for thermoplastic materials.

4.2. Results of experimental characterization

The relative tensile moduli of elasticity of the specimens extracted parallel and perpendicular to flow direction are depicted in Figs. 6 and 7. To obtain relative values, the measured values are normalized to density (ρ_{GF}=2.6 g/cm^3 and ρ_{resin}=1.14 g/cm^3) with the corresponding FVC of the sheet, determined by means of thermogravimetric analysis (cf. Table 3). Due to fiber orientation resulting from material flow tensile modulus of elasticity (E_t) of specimens extracted perpendicular to flow is significantly lower compared to E_t of specimens extracted in flow direction. In addition, stiffness of the material is slightly higher during the unloading portion of the cyclic tensile testing.

4.3. Effective elastic properties of the UPPH-based SMC composite

For the computations considered in this section, 0°- and 90°-oriented samples are used according to Sections 2 and 3.1. The isotropic engineering constants for the matrix material are given by $E_{\mathrm{M}} = 3.4$ GPa and $\nu_{\mathrm{M}} = 0.385$, cf. [28]. Regarding the fiber material, $E_{\mathrm{F}} = 73$ GPa and $\nu_{\mathrm{F}} = 0.22$ are considered according to [50]. For the fiber volume content c_{F}, the respective value for each sample according to Table 3 is used. Moreover, the orientation tensors of second and fourth order of the corresponding sample are used as input, cf. Section 4.1. Based on this data, the effective elastic stiffness is determined by the Hashin-Shtrikman (HS) two-step mean-field method and the results are documented in this section. The HS method presented yields two solutions based on the choice of the reference medium in the first step. Results for choosing the upper HS bound in the first step are denoted as HS$^+$, whereas HS$^-$ denotes results obtained by using the lower HS bound in the first step.

In order to compare simulation results with experimental data, the effective Young's modulus is determined by

$$\bar{E}(\boldsymbol{d}) = (\boldsymbol{d}\otimes\boldsymbol{d}\cdot\bar{\mathbb{C}}^{-1}[\boldsymbol{d}\otimes\boldsymbol{d}])^{-1}, \tag{13}$$

cf. [51]. The vectorial direction $\boldsymbol{d}$ is parametrized in spherical coordinates with respect to a unit sphere, i.e. $\boldsymbol{d} = \boldsymbol{d}(\vartheta,\varphi)$ and $\|\boldsymbol{d}\| = 1$. The quantities ϑ and φ denote the azimuth and the polar angle, respectively. The linear elastic behavior and, thus, $\bar{\mathbb{C}}$ is entirely defined by additional determination of

$$\bar{K}(\boldsymbol{d}) = \frac{1}{3}(\boldsymbol{I}\cdot\bar{\mathbb{C}}^{-1}[\boldsymbol{d}\otimes\boldsymbol{d}])^{-1}. \tag{14}$$

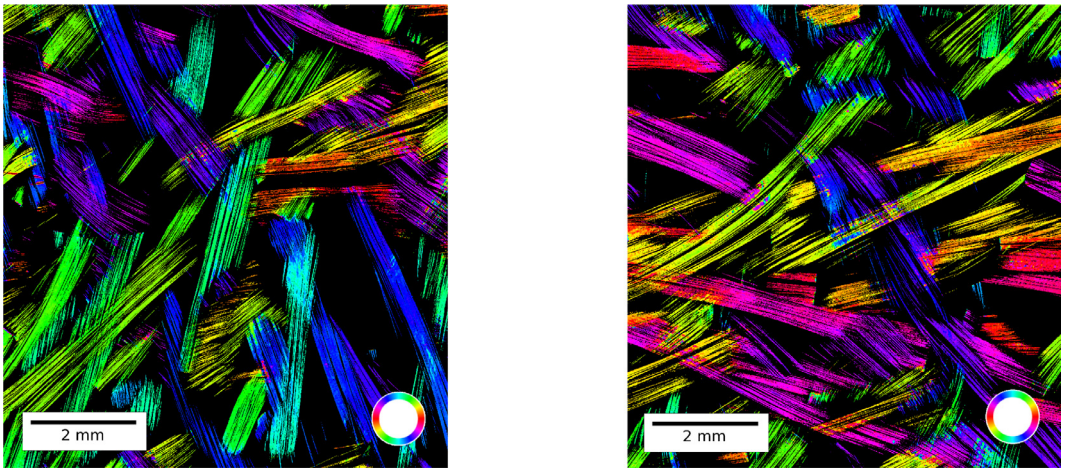

Fig. 3. Central plane over thickness of specimen 0°_1 (left) and specimen 90°_1 (right).

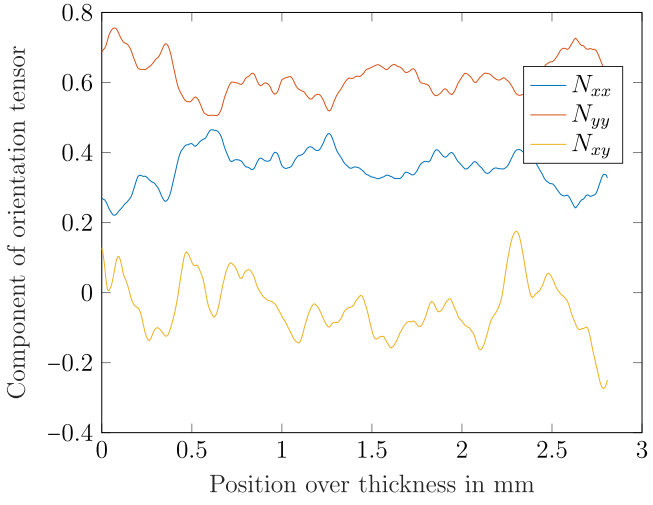

Fig. 4. Fiber orientation over thickness of specimen 0°_1 (y–axis of the specimen is parallel to flow direction).

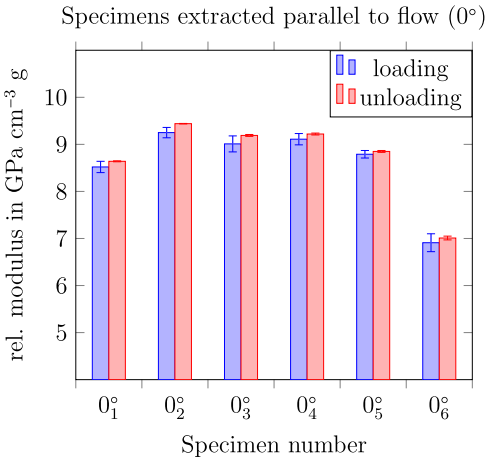

Fig. 6. Relative tensile modulus of elasticity of specimens extracted parallel to flow (0°) determined with strain measurements of loading and unloading portion, respectively.

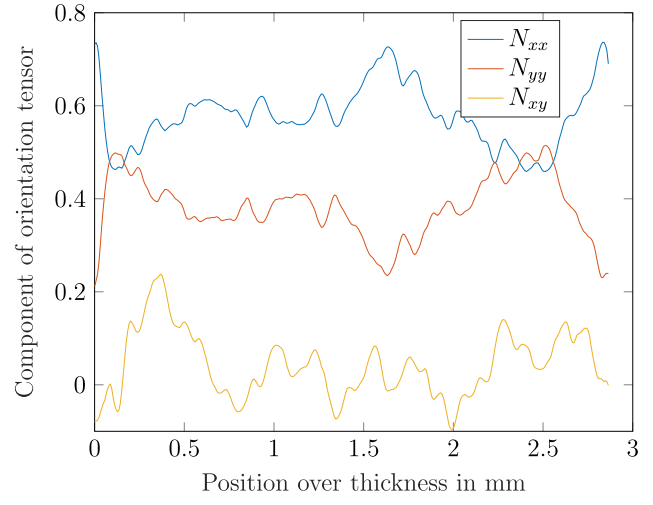

Fig. 5. Fiber orientation over thickness of specimen 90°_1 (y–axis of the specimen is perpendicular to flow direction).

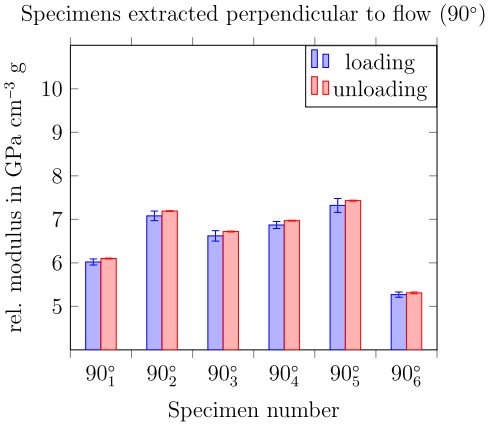

Fig. 7. Relative tensile modulus of elasticity of specimens extracted perpendicular to flow (90°) determined with strain measurements of loading and unloading portion, respectively.

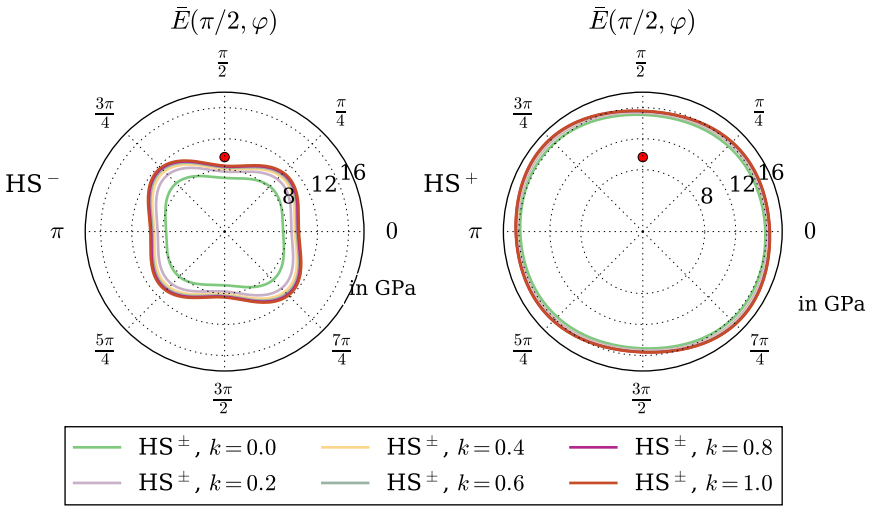

Fig. 8. Simulation results, computed by the HS$^-$ and the HS$^+$ mean-field method, compared to experimental data of the 90°_3 sample represented by the red dots. The orientation-dependent effective Young's modulus $\bar{E}(\boldsymbol{d})$ is depicted in the x-y–plane. The mean-field method is formulated in terms of a variable parameter k to investigate the influence of the reference stiffness on the predicted elastic material behavior.

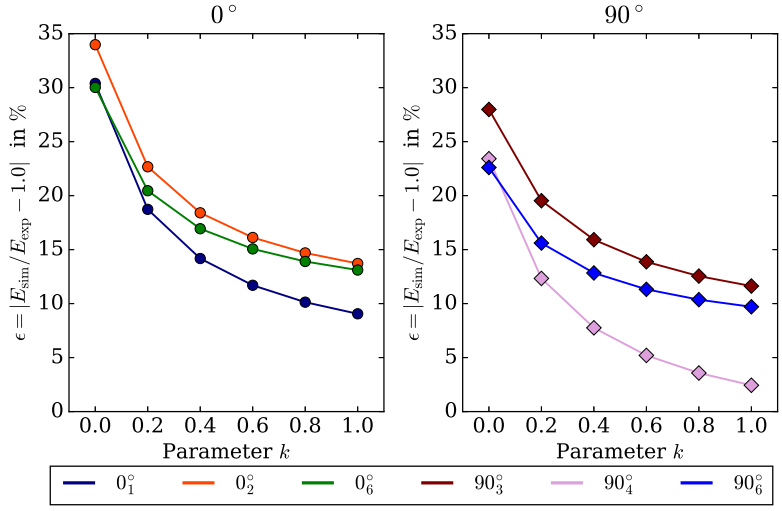

Fig. 9. Relative error between simulation results and experimental data for 0° and 90° samples for varying parameter k.

For a comparison with experimental data, here, only Young's modulus is considered. Regarding the measured Young's modulus, the corresponding effective value is given by $\bar{E}(\pi/2, \pi/2)$ with respect to the y-direction.

In Fig. 8, the contour plots of the orientation-dependent Young's moduli of the 90°_3 sample are shown. The results are depicted with respect to the x-y–plane corresponding to $\{\vartheta = \pi/2, \varphi\}$. The left diagram shows the results for the HS$^-$ method, whereas the results obtained by the HS$^+$ method are depicted in the right contour plot. Furthermore, the simulation results are shown for varying parameter k between 0 and 1 in five steps. Considering the tensile tests, the experimental data is given with respect to the y-direction corresponding to $\varphi = \pi/2$. Comparing the results for both methods, the HS$^-$ method yields a more precise prediction with respect to the experimental data than HS$^+$. This pronounced stiff behavior obtained by the HS$^+$ method is caused by the fiber stiffness in the first step. Since the phase contrast between matrix and fiber material is comparably high, this behavior is reasonable. Moreover, a more pronounced anisotropic behavior is computed for $\bar{E}(\boldsymbol{d})$ using the HS$^-$ instead of the HS$^+$ method. Especially, the HS$^-$ method shows a sensitive behavior regarding the choice of parameter k.

In order to investigate the influence of the parameter k on the effective elastic properties, the relative error between simulation results and experimental data is shown in Fig. 9 for 0° and 90° samples. Herein, only simulation results using the HS$^-$ method are considered. With increasing values of parameter k, the relative error decreases leading to $k = 1.0$ as smallest deviation. The choice $k = 1.0$ corresponds to using the fiber stiffness as reference stiffness in the second homogenization step. Thus, for the following investigations, the results are presented for $k = 1.0$.

In Fig. 10, the relative error between the predicted and measured Young's modulus is shown for all samples considered. Here, the experimental data obtained by tensile tests is considered.

In the left diagram, the results are shown for the 0° samples whereas, the right diagram shows the relative error for 90°-oriented samples. Considering all samples, the maximal relative error is nearly 18% whereas the smallest deviation is about 3%. As already shown in Figs. 6 and 7, the results with respect to the respective sample and the initial position

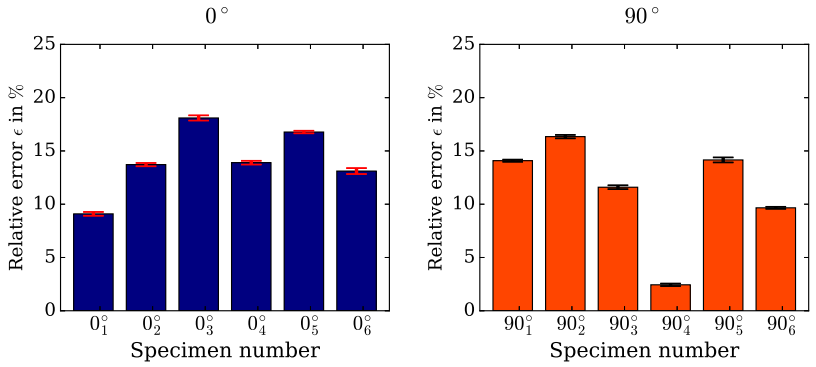

Fig. 10. Relative error between simulation results and experimental data for all 0° and 90° samples and $k = 1.0$.

on the plate are sensitive due to the scattering fiber volume content. If the scattering of the microstructure and the fiber volume content within the plate is known, the statistical scatter of the effective properties could be determined and compared with the corresponding mechanical properties, cf. [45].

5. Conclusions

In this work, an SMC composite based on glass fiber reinforced unsaturated polyester-polyurethane resin was considered. Samples were extracted from cured sheets in 0° and 90° with respect to the flow direction during the manufacturing process. The work mainly focused on the experimental characterization by tensile tests. Moreover, the microstructure was characterized by means of µCT scans. The resultant fiber orientation was used as input for a two-step mean-field method to compute the effective elastic behavior. Finally, the simulation results were compared to the experimental results. The following conclusions can be made:

Macrostructure characterization

- A higher fiber volume content led to elevated mechanical properties and higher stiffness of the specimens.
- Fiber orientation resulting from manufacturing of semi-finished material and mold filling affects tensile modulus of elasticity, leading to slightly anisotropic materials properties.
- In general, deviation between different stiffness measurements of one sample were extremely low (coefficient of variation <3%). However, lowest deviation resulted from properties determined with stress and strain values of unloading portion.

Microstructure characterization

- The orientation analysis based on the structure tensor [37] is suitable to process GF SMC material at a resolution of 8.04 µm per voxel.
- Orientation analyses prove that fiber distributions are slightly aligned to the flow direction.
- CT-scans show that fibers within the SMC material exist in bundles which are slightly dispersed on the surface. Moreover, there is a minor skin-core effect in orientation over thickness.

Effective material properties

- The variable reference stiffness enabled to adjust the method to the material class considered. This is especially favorable in terms of high phase contrast. In this case, choosing the more compliant material properties in the first step, and the stiffer fiber material in the second step yielded smallest deviations from experimental data.
- The highly heterogeneous microstructure yielded an anisotropic stiffness of the composite material.
- The effective Young's modulus was in good agreement with the experimental data obtained by the tensile tests. For most of the samples, the deviations were less than 15%.

Declaration of Competing Interest

The authors declare that they have no known competing financial interests or personal relationships that could have appeared to influence the work reported in this paper.

Acknowledgments

The research documented in this manuscript has been funded by the German Research Foundation (DFG) within the International Research Training Group "Integrated engineering of continuous-discontinuous long fiber reinforced polymer structures" (GRK 2078). The support by the German Research Foundation (DFG) is gratefully acknowledged. The authors also kindly acknowledge the Fraunhofer ICT in Pfinztal, Germany, with a special thanks to Dr.-Ing. D. Bücheler for his support to manufacture the SMC materials, and A. Heuer to carry out experimental characterization.

References

[1] P. Stachel, Serienfertigung mit Verbundwerkstoffen - AVK e.V. - Pressemitteilung, retrieved from: http://www.pressebox.de/inaktiv/avk-ev/Serienfertigung-mit-Verbundwerkstoffen/boxid/535921 (2012).
[2] The European Alliance for SMC/BMC, Life cycle assessment (LCA): SMC/BMC Light composite materials at their best, retrieved from: https://smcbmc-europe.org/publications.php (2013).
[3] The European Alliance for SMC/BMC, Design for success: a design & technology manual for SMC/BMC, retrieved from: https://smcbmc-europe.org/publications.php (2016).
[4] C. Lin, C. Weng, Simulation of compression molding for sheet molding compound considering the anisotropic effect, Polym. Compos. 20 (1) (1999) 98–113, doi:10.1002/pc.10338.
[5] T. Mei, M.R. Piggott, Mesostructure development during molding of sheet molding compounds, Polym. Compos. 17 (4) (2004) 548–555, doi:10.1002/pc.10645.
[6] D.G. Taggart, R.B. Pipes, J.W. Gillespie Jr, J.M. Whitney, Properties of SMC Composites: Report No CCM-79-1, 2020.
[7] K.T. Kim, Y.T. Im, Experimental study on physical properties of compression molded SMC parts under plane strain condition, Compos. Struct. 35 (2) (1996) 131–141, doi:10.1016/0263-8223(95)00158-1.
[8] S. Boylan, J.M. Castro, Effect of reinforcement type and length on physical properties, surface quality, and cycle time for sheet molding compound (SMC) compression molded parts, J. Appl. Polym. Sci. 90 (9) (2003) 2557–2571, doi:10.1002/app.12726.
[9] G. Lamanna, A. Ceprano, Mechanical characterization of sheet moulding composites for the automotive industry, Open Mater. Sci. J. 8 (1) (2014) 108–113, doi:10.2174/1874088X01408010108.
[10] A. Trauth, P. Pinter, K.A. Weidenmann, Investigation of quasi-static and dynamic material properties of a structural sheet molding compound combined with acoustic emission damage analysis, J. Compos. Sci. 1 (2) (2017), doi:10.3390/jcs1020018.
[11] E. Witten, T. Kraus, M. Kühnle, Composites market report - market developments, trends, outlook and challenges, retrieved from: https://www.carbon-composites.eu (2016).
[12] M. Hohberg, L. Kärger, F. Henning, A. Hrymak, Rheological measurements and rheological shell model considering the compressible behavior of long fiber reinforced sheet molding compound (SMC), Compos. Part A 95 (2017) 110–117, doi:10.1016/j.compositesa.2017.01.006.
[13] Y. Song, U. Gandhi, C. Pérez, T. Osswald, S. Vallury, A. Yang, Method to account for the fiber orientation of the initial charge on the fiber orientation of finished part

in compression molding simulation, Compos. Part A 100 (Supplement C) (2017) 244–254, doi:10.1016/j.compositesa.2017.05.021.
[14] Z. Chen, T. Huang, Y. Shao, Y. Li, H. Xu, K. Avery, D. Zeng, W. Chen, X. Su, Multi-scale finite element modeling of sheet molding compound (SMC) composite structure based on stochastic mesostructure reconstruction, Compos. Struct. 188 (2018) 25–38, doi:10.1016/j.compstruct.2017.12.039.
[15] J. Tham, T. Sabiston, A. Trauth, J. Lévesque, K. Weidenmann, K. Inal, The effect of tension compression asymmetry on modelling the bending response of sheet moulding compound composites, Compos. Part B 154 (2018) 157–165, doi:10.1016/j.compositesb.2018.07.058.
[16] M. Schemmann, J. Görthofer, T. Seelig, A. Hrymak, T. Böhlke, Anisotropic mean-field modeling of debonding and matrix damage in SMC composites, Compos. Sci. Technol. 161 (2018) 143–158.
[17] J. Görthofer, N. Meyer, T.D. Pallicity, L. Schöttl, A. Trauth, M. Schemmann, M. Hohberg, P. Pinter, P. Elsner, F. Henning, A. Hrymak, T. Seelig, K.A. Weidenmann, L. Kärger, T. Böhlke, Virtual process chain of sheet molding compound: Development, validation and perspectives, Compos. Part B 169 (2019) 133–147, doi:10.1016/j.compositesb.2019.04.001.
[18] T. Böhlke, F. Henning, A.N. Hrymak, L. Kärger, K. Weidenmann, J.T. Wood, Continuous-Discontinuous Fiber-Reinforced Polymers. An Integrated Engineering Approach., Hanser Fachbuchverlag, Munich, 2019.
[19] W. Voigt, Ueber die Beziehung zwischen den beiden Elasticitätsconstanten isotroper Körper, Annalen der Physik 274 (12) (1889) 573–587.
[20] A. Reuss, Berechnung der Fließgrenze von Mischkristallen auf Grund der Plastizitätsbedingung für Einkristalle, J. Appl. Math. Mech. 9 (1) (1929) 49–58.
[21] Z. Hashin, S. Shtrikman, A variational approach to the theory of the elastic behaviour of polycrystals, J. Mech. Phys. Solids 10 (4) (1962) 343–352, doi:10.1016/0022-5096(62)90005-4.
[22] A.V. Hershey, The elasticity of an isotropic aggregate of anisotropic cubic crystals, J. Appl. Mech.-Trans.ASME 21 (3) (1954) 236–240.
[23] E. Kröner, Berechnung der elastischen Konstanten des Vielkristalls aus den Konstanten des Einkristalls, Z. Phys. 151 (4) (1958) 504–518.
[24] T. Mori, K. Tanaka, Average stress in matrix and average elastic energy of materials with misfitting inclusions, Acta Metallurgica 21 (5) (1973) 571–574.
[25] V. Müller, Micromechanical Modeling of Short-fiber Reinforced Composites, KIT Scientific Publishing, Schriftenreihe Kontinuumsmechanik im Maschinenbau Nr. 6, 2016 Doctoral Dissertation. doi:10.5445/KSP/1000050760.
[26] H. Pettermann, H. Böhm, F. Rammerstorfer, Some direction-dependent properties of matrix-inclusion type composites with given reinforcement orientation distributions, Compos. Part B 28 (3) (1997) 253–265, doi:10.1016/S1359-8368(96)00055-8.
[27] B. Brylka, Charakterisierung und Modellierung der Steifigkeit von langfaserverstärktem Polypropylen, KIT Scientific Publishing, Schriftenreihe Kontinuumsmechanik im Maschinenbau Nr. 10, 2017 Doctoral Disseration. doi: 10.5445/KSP/1000070061.
[28] M.L. Kehrer, Thermomechanical Mean-Field Modeling and Experimental Characterization of Long Fiber-Reinforced Sheet Molding, KIT Scientific Publishing, Schriftenreihe Kontinuumsmechanik im Maschinenbau Nr. 15, 2019 Doctoral Dissertation. doi:10.5445/KSP/1000093328.
[29] M. Schemmann, S. Gajek, T. Böhlke, Biaxial tensile tests and microstructure-based inverse parameter identification of inhomogeneous SMC composites, in: Advances in Mechanics of Materials and Structural Analysis, Springer, 2018, pp. 329–342.
[30] H. Andrä, R. Grzhibovskis, S. Rjasanow, Boundary Element Method for Linear Elasticity with Conservative Body Forces, Springer, Berlin, Heidelberg, pp. 275–297. doi:10.1007/978-3-642-30316-6_13.
[31] M. Schneider, D. Merkert, M. Kabel, FFT-based homogenization for microstructures discretized by linear hexahedral elements, Int. J. Numer. Methods Eng. 109 (10) (2017) 1461–1489.
[32] F. Ernesti, M. Schneider, T. Böhlke, Fast implicit solvers for phase-field fracture problems on heterogeneous microstructures, Comput. Methods Appl. Mech. Eng. 363 (2020) 112793, doi:10.1016/j.cma.2019.112793.
[33] M. Schneider, An FFT-based fast gradient method for elastic and inelastic unit cell homogenization problems, Comput. Methods Appl. Mech. Eng. 315 (2017) 846–866.
[34] C. Truesdell, W. Noll, The non-linear field theories of mechanics, in: The Non-linear Field Theories of Mechanics, Springer, Heidelberg, Berlin, 2004, pp. 1–579.
[35] M. Silhavy, The Mechanics and Thermodynamics of Continuous Media, Springer Science & Business Media, Berlin, Heidelberg, 2013.
[36] A. Trauth, K.A. Weidenmann, Continuous-discontinuous sheet moulding compounds – effect of hybridisation on mechanical material properties, Compos. Struct. (2018), doi:10.1016/j.compstruct.2018.05.048.
[37] M. Krause, J.M. Hausherr, B. Burgeth, C. Herrmann, W. Krenkel, Determination of the fibre orientation in composites using the structure tensor and local x-ray transform, J. Mater. Sci. 45 (4) (2010) 888–896, doi:10.1007/s10853-009-4016-4.
[38] P. Pinter, S. Dietrich, B. Bertram, L. Kehrer, P. Elsner, K.A. Weidenmann, Comparison and error estimation of 3D fibre orientation analysis of computed tomography image data for fibre reinforced composites, NDT & E Int. 95 (2018) 26–35, doi:10.1016/j.ndteint.2018.01.001.
[39] W. Tsai, Moment-preserving thresolding: a new approach, Comput. Vis. Graph. Image Process. 29 (3) (1985) 377–393, doi:10.1016/0734-189X(85)90133-1.
[40] S.G. Advani, C.L. Tucker, The use of tensors to describe and predict fiber orientation in short fiber composites, J. Rheol. 31 (1987) 751–784, doi:10.1122/1.549945.
[41] T. Böhlke, K. Jöchen, R. Piat, T. Langhoff, I. Tsukrov, B. Reznik, Elastic properties of pyrolytic carbon with axisymmetric textures, Tech. Mech. Sci. J. Fundam. Appl. Eng. Mech. 30 (4) (2010) 343–353, doi:10.1016/j.mechmat.2009.08.007.
[42] A. Morawiec, J. Pospiech, Functions describing orientation correlations in polycrystalline materials, Text. Stress Microstruct. 19 (1–2) (1992) 67–74, doi:10.1155/TSM.19.67.
[43] K. Kanatani, Distribution of directional data and fabric tensors, Int. J. Eng. Sci. 22 (2) (1984) 149–164.
[44] P.A. Hessman, T. Riedel, F. Welschinger, K. Hornberger, T. Böhlke, Microstructural analysis of short glass fiber reinforced thermoplastics based on x-ray micro-computed tomography, Compos. Sci. Technol. 183 (2019) 107752, doi:10.1016/j.compscitech.2019.107752.
[45] A. Asadi, M. Miller, S. Sultana, R. Moon, K. TKalaitzidou, Introducing cellulose nanocrystals in sheet molding compounds (SMC), Compos. Part A 88 (2016) 206–215, doi:10.1016/j.compositesa.2016.05.033.
[46] A. Motaghi, A.N. Hrymak, Microstructure characterization in direct sheet molding compound, Polym. Compos. (2017), doi:10.1002/pc.24495.
[47] J.R. Willis, Variational and related methods for the overall properties of composites, Adv. Appl. Mech. 21 (1981) 1–78.
[48] L. Walpole, On bounds for the overall elastic moduli of inhomogeneous systems–I, J. Mech. Phys. Solids 14 (3) (1966) 151–162, doi:10.1016/0022-5096(66)90035-4.
[49] L. Walpole, On the overall elastic moduli of composite materials, J. Mech. Phys. Solids 17 (4) (1969) 235–251, doi:10.1016/0022-5096(69)90014-3.
[50] Granta Design, CES Edupack materials selector, (2016).
[51] T. Böhlke, C. Brüggemann, Graphical representation of the generalized Hooke's law, Tech. Mech. 21 (2) (2001) 145–158, doi:10.5445/IR/1000013749.